

Designing Outside the Box: Unlocking the Geometric Freedom of Melt Electrowriting using Microscale Layer Shifting

Ievgenii Liashenko, Andrei Hrynevich, and Paul D. Dalton*

Melt electrowriting, a high-resolution additive manufacturing technology, has so far been developed with vertical stacking of fiber layers, with a printing trajectory that is constant for each layer. In this work, microscale layer shifting is introduced through deliberately offsetting the printing trajectory for each printed layer. Inaccuracies during the printing of sinusoidal walls are corrected via layer shifting, resulting in accurate control of their geometry and mechanical properties. Furthermore, more substantial layer shifting allows stacking of fiber layers in a horizontal manner, overcoming the electrostatic autofocusing effect that favors vertical layer stacking. Novel nonlinear geometries, such as overhangs, wall texturing and branching, and smooth and abrupt changes in printing trajectory are presented, demonstrating the flexibility of the layer shifting approach beyond the state-of-the-art. The practice of microscale layer shifting for melt electrowriting enables more complex geometries that promise to have a profound impact on the development of products in a broad range of applications.

Melt electrowriting (MEW) is a high-resolution additive manufacturing technology with potential use in several areas including optics, electronics, textiles, and biomedical applications.^[1] It is based on a melt-extrusion 3D printing concept; however, the nozzle is raised above the collector, while the application of a high voltage maintains a thin molten jet between the two.^[2] MEW also has a substantially lower flow rate to the nozzle (typically $0.5\text{--}20\ \mu\text{L h}^{-1}$) which typically results in fiber diameters from 2 to 50 μm ;^[3] notably smaller than conventional

melt-extruded fibers. The smallest diameter MEW fibers reported to date are 0.8 μm .^[4]

Reinforcing frames made from MEW prints also have a substantial effect on the mechanical properties of hydrogels.^[5] MEW prints with a sinusoidal laydown pattern can render weak hydrogels into tough, flexible materials even though the overall volume fraction occupied by the reinforcing frame is low.^[6] The MEW fiber placement in particular greatly impacts the flexural properties for such soft network composites,^[7] and mechanically complex tissues such as heart valves are being designed and fabricated based on such principles.^[8]

To date, MEW research has involved the repeated stacking of individual fibers vertically upon each other,^[1,9] or deliberately misaligning each layer to induce a more


porous morphology through fiber suspension.^[10] Figure 1A and Video S1 in the Supporting Information shows that when printing above the critical translation speed (CTS), the electrified MEW jet lands on the collector/sample a slight distance behind the nozzle position. Due to this “jet lag,” fiber placement is substantially affected when the translation direction is changing while following nonlinear printing path, as it is in this study.^[11] Figure 1B shows a poly(ϵ -caprolactone) (PCL) fiber “wall” sinusoidally printed with identical printing path for each layer at the CTS ($180\ \text{mm min}^{-1}$) so that jet lag is minimal. Artifacts can be seen at a certain fiber layer height,^[9] and the black arrow in Figure 1B indicates this transition from ideal to non-ideal manufacturing conditions.

Normally, this printing defect at the CTS is accounted for by performing MEW at higher collector speeds,^[12] as exemplified in Figure 1B. Increasing the collector speed; however, increases the jet lag and results in greater deviation in printed pattern compared to the intended pattern, to the extent that at $2 \times \text{CTS}$ ($360\ \text{mm min}^{-1}$), the fiber wall has a significantly reduced sinusoidal form (Figure 1B; Videos S2 and S3, Supporting Information). An important observation for collector speeds above the CTS, is the inward tilting of the fiber wall towards the centerline of the printed structure. Based on collection speeds used in previous papers,^[6,12] Figure 1B ($1.25 \times \text{CTS}$) is most representative of this situation and is adopted here, and a rendering of this effect is presented in Video S2 in the Supporting Information. For the remainder of the study, all printing parameters were fixed with only the printing path altered.

I. Liashenko
Department of Chemical Engineering
Universitat Rovira i Virgili
Av. dels Països Catalans 26, Tarragona 43007, Spain

I. Liashenko
Catalonia Institute for Energy Research – IREC
Sant Adrià de Besòs 1, Pl 2, Barcelona 08930, Spain

I. Liashenko, A. Hrynevich, Prof. P. D. Dalton
Department of Functional Materials in Medicine and
Dentistry and Bavarian Polymer Institute
University Hospital of Würzburg
Pleicherwall 2, Würzburg 97070, Germany
E-mail: paul.dalton@fmz.uni-wuerzburg.de

 The ORCID identification number(s) for the author(s) of this article can be found under <https://doi.org/10.1002/adma.202001874>.

© 2020 The Authors. Published by WILEY-VCH Verlag GmbH & Co. KGaA, Weinheim. This is an open access article under the terms of the Creative Commons Attribution License, which permits use, distribution and reproduction in any medium, provided the original work is properly cited.

DOI: 10.1002/adma.202001874

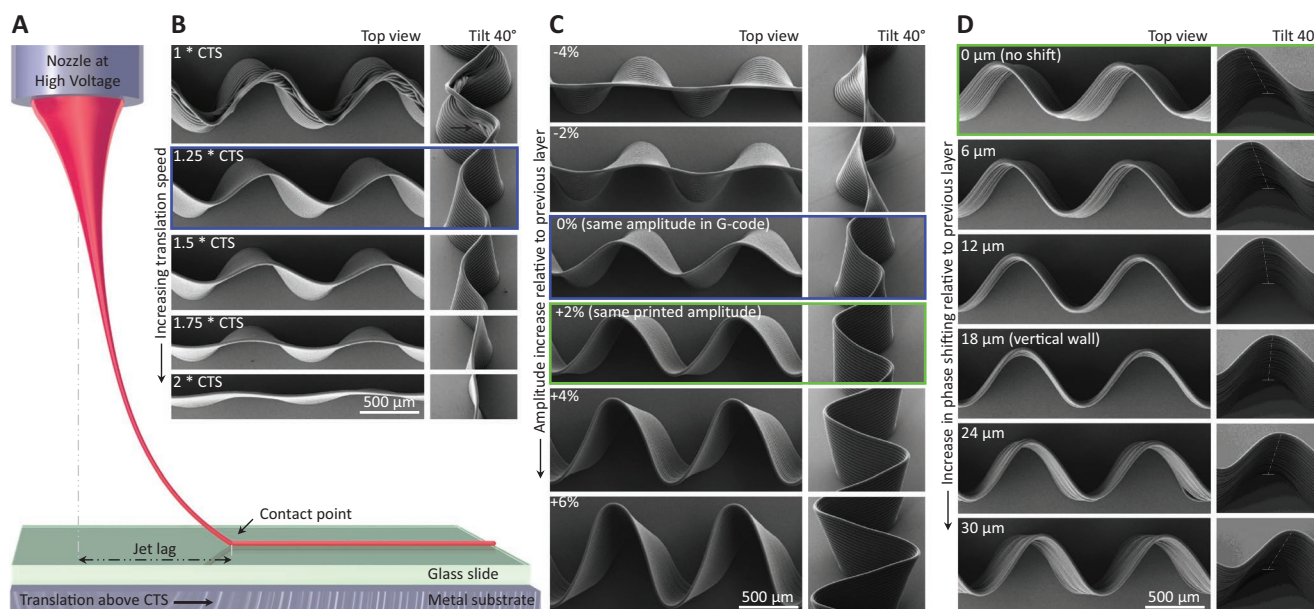


Figure 1. Effect of microscale layer shifting on tilting of the MEW fiber wall. A) Schematic of the electrified molten jet, highlighted with the jet lag to show that the fiber path and the printing path can be different when changing directions. B–D) SEM images of fiber walls fabricated with: B) identical printing paths and different collector speeds; C) an identical collector speed of $1.25 \times$ CTS but with an increase/decrease in amplitude layer-on-layer; D) identical 2% layer-on-layer increase in amplitude as well as various phase shifts of the printing path. Videos S3–S6 in the Supporting Information visualize these alterations. Figure S3 in the Supporting Information additionally shows how a smooth change in collector speed, amplitude, and layer-on-layer offset affects the tilting and overall geometry of sinusoidal walls.

A layer-by-layer offset for the printing path amplitude can be used to affect the inwards tilting of the MEW fiber wall. When the printing path amplitude is increased by 2% of the first layer amplitude ($15 \mu\text{m}$ per layer), the MEW walls were more vertical (Figure 1C). Figure S1 and Video S6 in the Supporting Information show similar effect of 2% layer-on-layer increase for sinusoidal walls with different amplitudes. When increasing the amplitude of the printing path by 4% or 6% on the previous layer, the fiber wall tilts outward. (Figure 1C; Video S4, Supporting Information). As would be expected, the reduction in amplitude resulted in more inwards tilting for -4% and -2% layer-on-layer samples.

A sinusoidal fiber wall was also found to tilt forward (i.e., in the direction of the direct-writing), shown in Figure 1D. However, it is possible to shift the phase of the sinusoidal printing path for each subsequent layer backward to correct this imperfection. Figure 1D and Video S5 in the Supporting Information shows a series of different phase shifts for the printing path, ranging from no shifting to $30 \mu\text{m}$ per layer. Forward tilting of the sinusoid could be corrected to a near-vertical wall using $12\text{--}18 \mu\text{m}$ phase shifts in the printing path for each subsequent layer. Similarly, backwards tilting of the sinusoid wall can be induced by shifting the phase of the sinusoidal printing path above $18 \mu\text{m}$ per layer (Figure 1D).

Such adjustment to each fiber layer path (i.e., microscale layer shifting) allows to arbitrarily control the tilt of sinusoidal walls (as shown on Figure S2 in the Supporting Information), and would be expected to impact the mechanical properties of the printed structure. Since there is variance in the inwards/outwards tilting, each fiber would experience a different force depending on its position within the fiber wall. Mechanical

testing (Figure 2) used samples where the first layer had the same pattern, and subsequent layers had different magnitudes of amplitude increase. Sinusoidally-printed walls all had toe and heel regions in their tensile responses; however, the shape of this curve greatly depended on the microscale shifting and whether it was inwards or outwards tilting.

For inwards tilting, the upper fiber is initially loaded while for outwards tilting the lower fiber has the initial load. However, for a 2% layer-on-layer increase for each printing path amplitude, the sinusoidal wall is near-vertical. When this sample (pink-color indicated) is stretched, the tensile load is nearly equally distributed across the wall, and there is substantial deformation before the resistance to strain starts growing with its maximal rate. For this sample, a linear zone (pink arrowed) is observed, and corresponds to an elastic modulus of 115 MPa that is lower than the straight MEW fiber control (190 MPa) and the values found previously for this medical-grade PCL ($154 \pm 23 \text{ MPa}$).^[13] As an indicator, the standard approach to MEW for sinusoidal fibers results in a force–strain curve shown in light blue. Under these printing circumstances, there are fibers within the sinusoidal wall that are loaded differently depending on their height in the fiber wall.

The capability to nonvertically stack MEW layers using microscale shifting increases the geometric freedom for the fabrication of structures, as it addresses an inherent feature of additive manufacturing. For example, walls of stacked MEW fibers can be tilted to varying degrees, by offsetting each layer with changes in the printing path. Notably, horizontal MEW fiber stacking is possible (Figure 3A), allowing the fabrication of overhanging MEW structures without using supports. In this instance, ten straight fibers were first printed, and the next

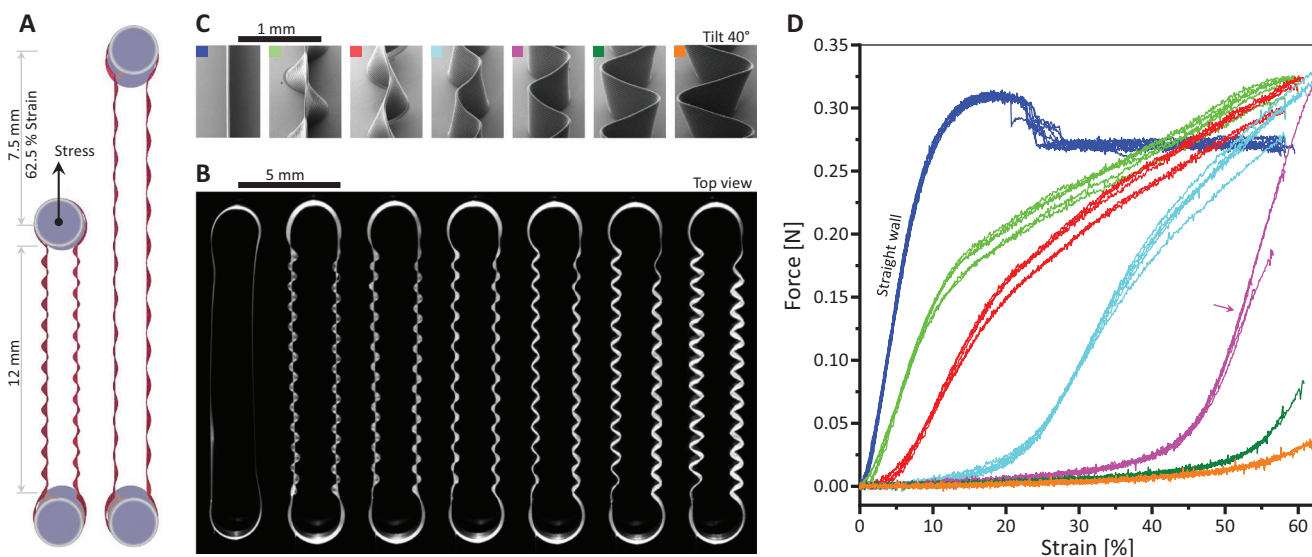


Figure 2. Tensile testing of sinusoidal fiber walls with controlled inwards/outwards tilting. A) Schematic of the “chain” style tensile testing approach that avoids sample slippage. B) Stereomicroscopy photograph and C) SEM image of the sinusoidal fiber walls used for tensile testing. Each sinusoidal wall comprised 20 fiber layers, thus the difference in tensile properties across samples is solely attributed to the deliberate placement of fiber layers. D) Force–strain curves are presented for these samples shown in (B),(C). Notably, the (pink-arrowed) sample with the most vertical walls had a similar linear slope to the straight fiber control. The 62.5% strain corresponds to the maximum limit of 7.5 mm in displacement.

ten printing paths shifted away from the centerline, resulting in a fiber depositing towards the side of the previous one. The degree of shifting allowed to precisely control the tilt angle of top ten layers (shift values are detailed in Table S1 in the Supporting Information). In the instance of 90° overhangs, it is important to note that a substantial offset is required (625 μm) to overcome the electrostatic attraction of the jet to the top of the previously deposited fiber.

Similarly, branching walls were printed by alternating the offset in printing path in opposite directions relative to the fiber wall centerline. The wall is composed of ten straight layers and top twenty tilted layers, thus making ten layers per branch (Figure 2B). Importantly, tilted layers were alternated between branches to ensure equal height growth (and thus electrical field gradient), during printing. Similar to overhangs, by pre-setting varying shift values it was possible to control the angle between branches. Triple-branched walls are also possible (Figure S5, Supporting Information).

Furthermore, the same approach used for printing double- and triple-branched walls can be employed for wall texturing (Figure 3C) by presetting small shift values, thus not reaching the separation of alternating fibers into “branches.” Such texturing of the MEW wall could be used for (i) wall reinforcement (against bending), (ii) guiding cell growth with the grooves, or (iii) to compensate for the local increase in heights when two walls cross (the textured wall is lower compared to normal one, even though the same number of layers are used).

Figure 3E shows scanning electron microscopy (SEM) images of complex MEW fiber walls inspired by nature (e.g., leaves, seaweed, liana) and composed of twenty fibers layers. To highlight the geometrical flexibility provided by layer shifting, three types of geometries depict how straight and sinusoidal layers can be smoothly morphed into a single fiber wall (additional views can be found in Figure S4 in the Supporting Information).

Expanding on the previous samples, Figure 3D shows an abrupt change in translation trajectory fabricating a “multiphase fiber wall,” where a straight wall was printed atop of a sinusoidal vertical wall. This also extends to the printing of several different MEW structures, including a multiphase wall comprising two sinusoids with different amplitudes (Figure 3D; Figure S6, Supporting Information). Multiphase walls could be used for achieving “step-function” mechanical properties, thus allowing to fine-tune the force–strain curve of the wall beyond what is already demonstrated in Figure 2D. This is particularly pertinent for soft network composites that are attempting to replicate the mechanical properties of soft tissue such as heart valves^[8] or ligaments/tendons.^[6] In such a “reverse engineering” approach, the desired mechanical properties are defined by the tissue of interest and the appropriate combination of fiber placement is then established.

To demonstrate how microscale layer shifting can facilitate fabrication of microstructures, small domes, shown in Figure 3F, were printed with forty layers at $1.25 \times$ CTS. The uppermost structure was printed using 0.5 mm constant radius trajectory but resulted into a truncated cone due to the shape change associated with jet lag. Dome structures can be fabricated with various degrees of taper by continuously updating the trajectory radius as a function of layer number. As a demonstration, radius was varied both linearly and periodically (sinusoidally) to obtain different wall inclinations and “vase-like” geometries.

The implications of this new geometric design capability for MEW include the ability to fabricate new biomedical materials such as scaffolds for tissue engineering. Such MEW designs to date are almost exclusively based on straight fibers made into square “box-shaped” MEW scaffolds. The majority of MEW is also performed with linear movement between the nozzle and collector, resulting in straight fibers. Exceptions to both of these

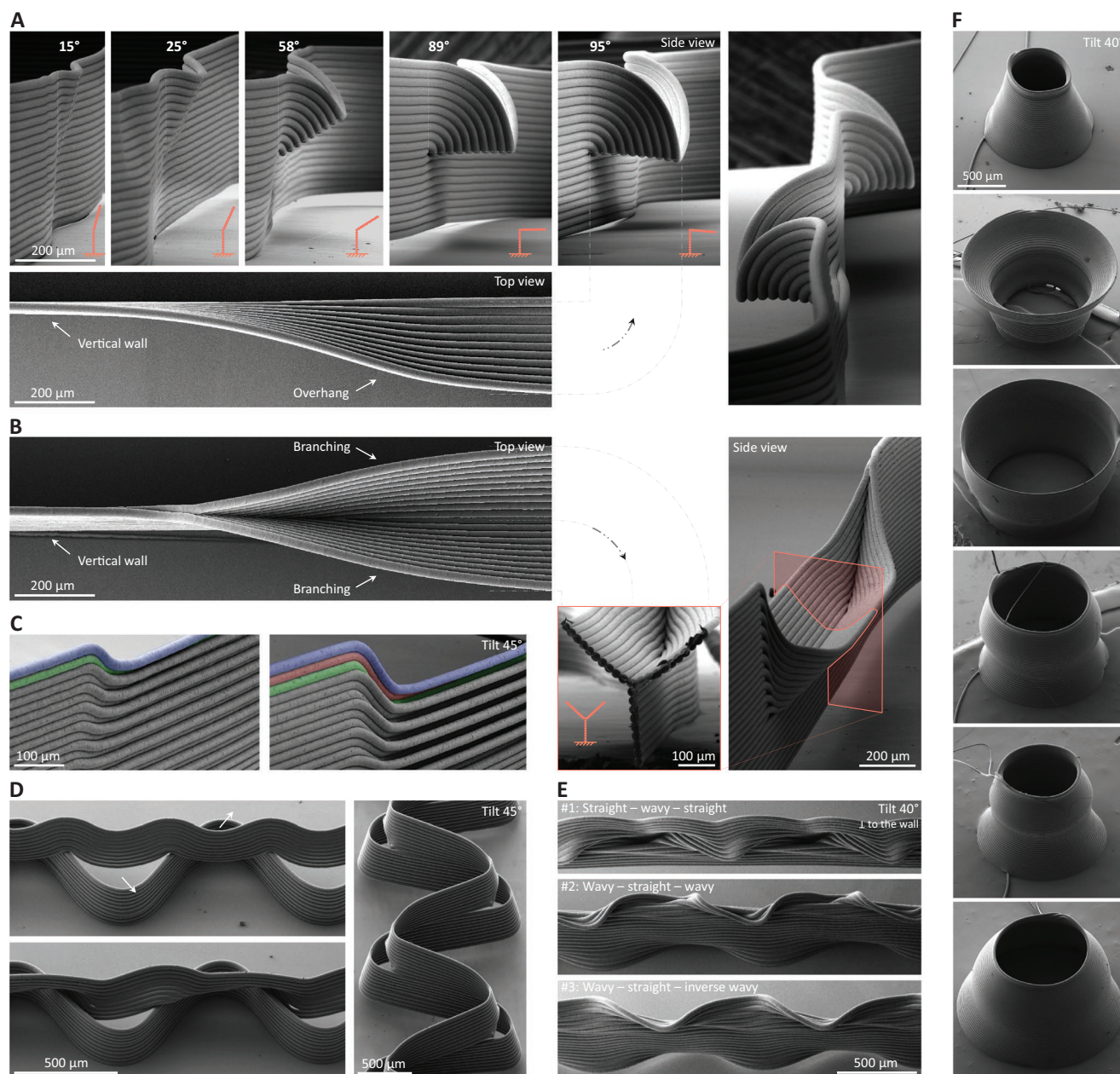


Figure 3. SEM images of novel complex geometries enabled by controlled layer shifting. A) Overhangs with increasing tilt ultimately allow horizontal printing without supporting/sacrificial structure. B) Branching of fiber wall into two overhangs. C) Microscale texturing allows fabricating grooves and local control of the wall height. D) Multiphasic walls created by an abrupt change in printing trajectory, to enable highly tunable “step-function” mechanical properties, beyond those presented in Figure 2. Openings/pores present another opportunity in designing advanced scaffolds (Figure S6, Supporting Information). E) Nature-inspired walls where sinusoidal and straight fiber layers are smoothly morphed producing three wall designs. Figure S4 in the Supporting Information shows other views of the same walls highlighting their geometrical complexity. F) Microscopic domes (“micro-pottery”) fabricated with different taper using layer shifting principles.

points are those MEW prints intended for use in the heart tissue engineering, since they have to undergo cyclic and complex mechanical loading.^[14] Auxetic MEW prints and injectable scaffolds with hexagonal microstructure have been developed as heart patches, whereas soft network composites are being investigated for heart valve replacement.^[8]

Building on such complex sinusoidal geometries, it is now possible that different MEW fiber walls can be tilted, as

exemplified with a triangle-pore scaffold (Figure 4A). Each side of this triangle pore has: (1) vertical (indicated green), (2) inward tilting (red), and (3) outward tilting (blue) fiber walls. Triangle-pore scaffolds have been previously reported,^[6] although in this instance the fiber wall tilting should alter the mechanical properties when the material is stretched in different directions, similar to Figure 2. For applications involving repetitive cyclic loading; however, a more elastomeric polymer would especially

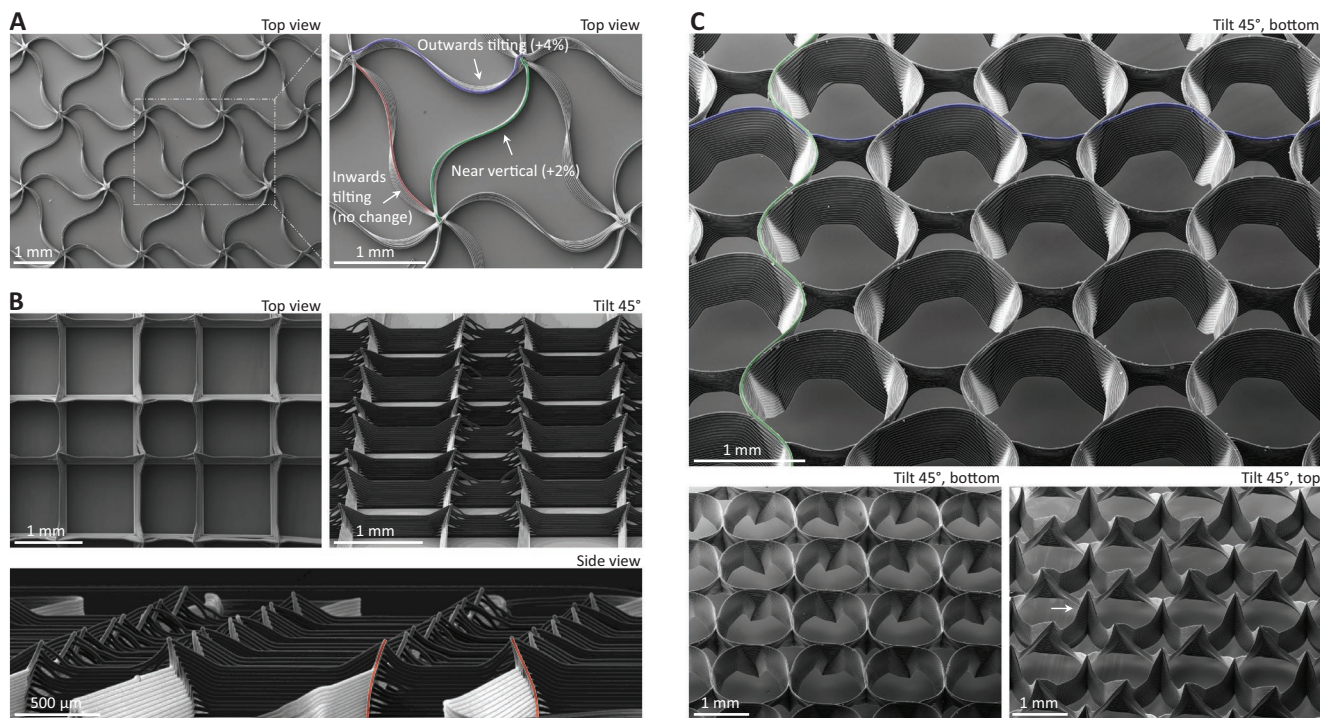


Figure 4. A) SEM image of MEW scaffold, with the magnified view showing that each edge of the triangle-shaped pore is printed with either 0%, 2%, or 4% increase in amplitude. This accordingly affects the tilting of the wall from inwards, near vertical, and outwards, indicated by false-coloring red, green, and blue respectively. B) MEW box scaffolds designed with variable wall tilting, false-colored red lines indicating the tilting of two fiber intersection points. C) SEM image of underneath a MEW scaffold with circular pores made by combining sinusoidally deposited fibers (two are exemplified with blue and green false-coloring). There are four parts of the circular pore which have double the quantity of fibers, and make a corresponding four fiber “peaks” on the upper side. Other views of the same scaffold are available in Figure S10 in the Supporting Information, highlighting its geometrical complexity.

take advantage of microscale layer shifting. Several chemically- and physically crosslinked polymers have been developed for MEW.^[15,16] The primary challenge with processing such polymers is reducing thermal crosslinking so that the printing conditions remain stable with time.^[16]

The concept of straight fiber wall tilting (shown in Figure 3A) was also exploited for fabricating box-shaped structures. These are the most common MEW geometrical structures reported^[3,17] and, up until now, are fabricated with straight, vertical walls. Figure 4B shows how the morphology is altered when the fiber walls are tilted, where variable pore sizes result from crossing tilted walls. False-colored imaging of the pores is used to highlight the overall patterning effect that results (Figure S8, Supporting Information).

The sinusoidal patterns shown in Figures 1 and 2 can also be used to fabricate circular pore MEW prints when opposite sinusoidal peaks are aligned and crossing points are precisely controlled. Figure S9 in the Supporting Information shows a five-layer MEW print that combines the sinusoidal fiber walls into a uniform and reproducible circular pore scaffold. Figure 4C shows three views of the same circular pore scaffold design (made of twenty layers), highlighting its geometrical complexity. While circular pore design is clearly visible from tilted view taken from the bottom of the scaffold, top view emphasizes the rapidly growing peaks at the four locations where the circular pores intersect with each other (Figure 4C; white arrow). Additional views of the same circular scaffold

can be found in Figure S10 in the Supporting Information. All printed scaffolds can be readily handled, with an example shown in Video S7 in the Supporting Information.

In summary, we demonstrate how layer positioning inaccuracies that occur within MEW due to jet lag can be corrected by updating the printing path for each deposited layer. Such microscale layer shifting can be used to layer fibers in a nonvertical manner, for example, to create overhangs without support structures, wall branching and texturing, as well as nature-inspired designs. As sinusoidal MEW printing substantially affects the mechanical properties of soft network composites, microscale layer shifting can substantially alter their mechanical properties. “Primitive” lines and boxed-shaped structures have generally been used in MEW since it was not previously known how to deliberately tilt walls to obtain more complex features. The electrostatic attraction of fibers to previously deposited ones also results in an autofocusing effect that tends to result in vertical MEW fiber walls. Overcoming this with microscale layer shifting is therefore an extra and powerful design approach for the fabrication of highly resolved and tailor-designed MEW products that have utility in a spectrum of value-added applications.

Experimental Section

Materials: Pellets of PURAC PC-12 Corbion PCL were purchased and used as received after appropriate storage.

MEW Conditions: A custom-built MEW printer, used for several other studies was used in this study. All printing parameters are stable throughout, once a translation speed of $1.25 \times \text{CTS}$ was established. A heating temperature of 87°C was used to melt the PCL, while an applied pressure of 1.2 bar forced the melt to a flat-tipped stainless steel nozzle of 22 gauge protruded ≈ 0.7 mm from the printhead. The collector distance was set to 3.5 mm, a high voltage of +5.75 kV was applied to the nozzle, while -1.5 kV was applied to the metal collector. MEW fibers were deposited onto glass slides (1 mm thick) positioned atop the metal collector. These parameters resulted in a CTS (i.e., jetting speed) of $180\text{--}230$ mm min^{-1} , which is variable due to daily changes in both the polymer and environmental conditions (ranging $19\text{--}22^\circ\text{C}$ and $35\text{--}42\%$ RH). Before each printing session, the jet was established/stabilized for more than 5 min to reach a steady state, after which CTS was measured and used to define the translation speed ($1.25 \times \text{CTS}$), resulting in fiber diameters of ≈ 25 μm . This approach of setting translation speed as a function of CTS allowed to decouple the effect of microscale layer shifting from small variations of CTS. The microscale layer shifting approach was repeatable and stable (further examples—Figure S11, Supporting Information), given that all other printing parameters are constant (CTS, fiber diameter, collector distance, etc.). Circular pore scaffolds required the most care as slight changes in the CTS caused a jet lag change that required recalibration of the G-code.

Printing geometries were controlled solely by the definition of the translation trajectory performed by the XY stage, while other printing parameters were fixed. Translation trajectory and speed were preset through the G-code. Translation trajectory typically varied as a function of layer number and was used to deliberately offset arriving fiber placement onto previously-deposited one, and allowed printing nonvertical features. Unless indicated, a total of twenty fiber layers were printed into a fiber wall. The printing paths used for all experiments shown in this study are given in Table S1 in the Supporting Information.

SEM Imaging: MEW structures were sputter-coated with approximately 4 nm of Pt using a Leica EM ACE600 system to improve imaging resolution. SEM images were taken with a Zeiss Crossbeam 340 with a secondary electron detector and acceleration voltages of 5–15 kV. Most samples were imaged directly on the glass collector, while the scaffold with circular pores was manually detached and imaged both from top and bottom for better showcasing its complex geometry (Figure 4C; Figure S7, Supporting Information). Similarly, circular domes were detached using tweezers and positioned on sticky carbon tape for imaging. Cross-section of walls was obtained by carefully cutting the sample with scissors and fixing on adhesive tape so that no deformation of printed structures was observed.

Mechanical Testing: MEW samples for tensile testing were fabricated using the design shown in Figure 2B and with the printing paths provided in Table S1 in the Supporting Information. “Chain-like” tensile testing samples were required over standard clamp-based testing, as the small diameter MEW fibers are difficult to grip/glue in the mechanical testing equipment without generating artifacts. Samples were detached from the glass slide after printing, and manually hooked over loops in the tensile tester (ElectroForce 5500, TA Instruments, USA). The length of sinusoidal wall was 12 mm and total displacement reached was 7.5 mm (a fixed limit of the micromechanical tester). Variations in sample mounting were corrected by shifting the strain axis while the measured force takes into account both sinusoidal walls in each test sample. Data are presented as force versus strain, due to difficulties in calculating the cross-sectional area (and hence stress) of the sinusoidal and tilting fiber walls.

Supporting Information

Supporting Information is available from the Wiley Online Library or from the author.

Acknowledgements

I.L. and A.H. contributed equally to this work. The preliminary research by Almoatazbellah Youssef, SEM assistance from Dr. Philipp Stahlhut, and proof-reading by Prof. Robert Luxenhofer is valued. Financial assistance from the Volkswagen Foundation (grant 93417) is acknowledged while I.L. appreciates financial support from Erasmus+ Traineeship Programme, EIT KIC InnoEnergy PhD School and from Generalitat de Catalunya (grant 2017FI_B_01202 and Llabor grant #26/2019). The German Research Foundation (INST 105022/58-1 FUGG) funded the Zeiss Crossbeam CB 340 SEM used in this study.

Conflict of Interest

The authors declare no conflict of interest.

Keywords

3D printing, additive manufacturing, biomaterials, electrohydrodynamics, melt electrospinning writing

Received: March 18, 2020

Revised: April 17, 2020

Published online: May 27, 2020

- [1] T. M. Robinson, D. W. Hutmacher, P. D. Dalton, *Adv. Funct. Mater.* **2019**, *29*, 1904664.
- [2] A. G. Marin, D. Lohse, *Phys. Fluids* **2010**, *22*, 122104.
- [3] A. Hrynevich, B. S. Elci, J. N. Haigh, R. McMaster, A. Youssef, C. Blum, T. Blunk, G. Hochleitner, J. Groll, P. D. Dalton, *Small* **2018**, *14*, 1800232.
- [4] G. Hochleitner, T. Jungst, T. D. Brown, K. Hahn, C. Moseke, F. Jakob, P. D. Dalton, J. Groll, *Biofabrication* **2015**, *7*, 035002.
- [5] J. Visser, F. P. W. Melchels, J. E. Jeon, E. M. van Bussel, L. S. Kimpton, H. M. Byrne, W. J. A. Dhert, P. D. Dalton, D. W. Hutmacher, J. Malda, *Nat. Commun.* **2015**, *6*, 6933.
- [6] O. Bas, D. D'Angella, J. G. Baldwin, N. J. Castro, F. M. Wunner, N. T. Saïdy, S. Kollmannsberger, A. Reali, E. Rank, E. M. De-Juan-Pardo, D. W. Hutmacher, *ACS Appl. Mater. Interfaces* **2017**, *9*, 29430.
- [7] O. Bas, I. Catelas, E. M. De-Juan-Pardo, D. W. Hutmacher, *Adv. Drug Delivery Rev.* **2018**, *132*, 214.
- [8] N. T. Saïdy, F. Wolf, O. Bas, H. Keijidener, D. W. Hutmacher, P. Mela, E. M. De-Juan-Pardo, *Small* **2019**, *15*, 1900873.
- [9] F. M. Wunner, M. L. Wille, T. G. Noonan, O. Bas, P. D. Dalton, E. M. De-Juan-Pardo, D. W. Hutmacher, *Adv. Mater.* **2018**, *30*, 1706570.
- [10] B. L. Farrugia, T. D. Brown, Z. Upton, D. W. Hutmacher, P. D. Dalton, T. R. Dargaville, *Biofabrication* **2013**, *5*, 025001.
- [11] G. Hochleitner, A. Youssef, A. Hrynevich, J. N. Haigh, T. Jungst, J. Groll, P. D. Dalton, *BioNanomaterials* **2016**, *17*, 159.
- [12] F. Tourlomousis, C. Jia, T. Karydis, A. Mershin, H. Wang, D. M. Kalyon, R. C. Chang, *Microsyst. Nanoeng.* **2019**, *5*, 15.
- [13] G. Hochleitner, *PhD Thesis*, University of Würzburg, OPUS Würzburg, Germany **2018**.
- [14] S. Mori, J. T. Tretter, D. E. Spicer, D. L. Bolender, R. H. Anderson, *Clin. Anat.* **2019**, *32*, 288.
- [15] a) F. Chen, G. Hochleitner, T. Woodfield, J. Groll, P. D. Dalton, B. G. Amsden, *Biomacromolecules* **2016**, *17*, 208; b) G. Hochleitner, E. Fursattel, R. Giesa, J. Groll, H. W. Schmidt, P. D. Dalton, *Macromol. Rapid Commun.* **2018**, *39*, 1800055.
- [16] D. Nahm, F. Weigl, N. Schaefer, A. Sancho, A. Frank, J. Groll, C. Villmann, H.-W. Schmidt, P. D. Dalton, R. Luxenhofer, *Mater. Horiz.* **2020**, *7*, 928.
- [17] K. F. Eichholz, D. A. Hoey, *Acta Biomater.* **2018**, *75*, 140.